Kragujevac Journal of Mathematics
Volume 50(10) (2026), Pages 1663–1683.

NUMERICAL MODELING OF LAMINAR CASSON FLUID FLOW IN ECCENTRIC ANNULAR ENTRANCE REGIONS

AMANY M. ATEIA[1] AND OSAMA H. GALAL[2]

Abstract. The laminar flow of an incompressible Casson fluid in the entrance region of an eccentric annulus was analyzed numerically. Such asymmetric annular structures are critical in applications like drilling, heat exchangers and biomedical simulations. The Casson fluid model, which is relevant for biological (e.g., blood), industrial (e.g., drilling fluids) and environmental (e.g., mudflows) systems, was investigated using the Finite Difference Method (FDM) with variable mesh size. The Navier-Stokes equations in bipolar coordinates were solved to calculate pressure gradients and axial velocities for varying radius ratios S, relative eccentricities e and yield stress values τ_D. The results for the entrance region, which were validated against the literature on fully developed flow, showed an accuracy of 97.89% to 99.68%. The entrance region pressure gradient exceeded the fully developed zone by 6.16 to 50.52 times, while the axial velocity ranged from 43.75% to 53.65% of its fully developed value. These findings underscore the importance of entrance region dynamics in engineering design.

1. Introduction

In heat exchangers, well drilling, and plastic extrusion, flow in the entrance region of concentric and/or eccentric annuli is important from an industrial standpoint. In engineering, however, the amount of power required to pump fluids through such systems is critical. The two factors that determine how much power is required to pump an incompressible fluid are the volumetric flow rate and the pressure drop. However, the pressure drop in the entrance region is greater than in the fully developed zone due to the acceleration of the fluid motion and the higher velocity gradients at the

Key words and phrases. Non-Newtonian flow, variable mesh size, eccentric annulus, Casson fluid, entrance region.

https://doi.org/10.46793/KgJMat2610.1663A

Received: September 07, 2024.

Accepted: April 27, 2025.

wall within this region. Since the fully developed pressure drop for the entire flow zone is used in the design calculations, the pumping power is underestimated. As a result, estimating the excess pressure gradient at the entrance region relative to the fully developed one is critical. In addition, the Casson fluid model is often used to describe the flow behavior of non-Newtonian fluids with yield stress, such as blood, chocolate, and certain industrial slurries [1]. It finds applications in biomedical engineering to model blood flow in vessels [2], in food processing to optimize the handling of viscous products such as chocolate [3] and in drilling operations to predict the behavior of muds and cement pastes [4]. This model helps engineers design efficient systems by accurately capturing the fluid's resistance to flow until a critical stress is reached [5].

However, numerous studies on laminar incompressible flow have focused on the entrance region of the concentric annular duct. For instance, an early work conducted theoretical studies on the velocity distribution, pressure drop and hydrodynamic entry length of pipes with annular space [6]. In addition, using the Casson stress-strain relation as a guide, the Runge-Kutta method was used to ascertain how blood flows in the entrance region of annuli [1]. The Finite Difference Method (FDM) was used to solve the axial, incompressible, isothermal, laminar and steady flow of a power-law fluid in a concentric annulus [3]. The entrance region for Herschel-Bulkley and Bingham non-Newtonian fluids in concentric annuli with a rotating inner wall and a stationary outer one was studied using the FDM [7, 8]. Recent studies have extended this focus to include advanced non-Newtonian models, such as the exploration of temperature-dependent thermophysical properties under bioconvection effects [9] and heat transport in Casson fluid flows within Darcy-Forchheimer media [10]. In addition, the entrance effects in concentric rings with inner ring rotation for the blood model Casson non-Newtonian fluid were also investigated [2]. They also investigated how the Casson fluid affects heat and mass transmission as the inner walls of the concentric annuli moved [11]. The non-Newtonian Bingham fluid was also investigated in the entry region of the annular space between two rotating coaxial cylinders [12].

On the other hand, several researchers have studied the problem of eccentric annuli in detail. Examples include the study of non-Newtonian fluid in eccentric annuli for highpolymer aqueous solutions of CMC, HEC, and MC [13]. The yield-power law fluids'velocity and viscosity profiles were derived using FDM by solving the governing laminar flow equation [4]. In their innovative method [14], the laminar eccentric annular flow of non-Newtonian fluids was investigated, where the eccentric annulus is represented by an infinite number of concentric annuli with varied outer radii. A fully developed laminar flow of a Newtonian fluid across an eccentric annulus was investigated computationally and experimentally [15]. In addition, when Newtonian and non-Newtonian fluids were examined in an eccentric annulus, the case of inner cylinder rotation was also taken into consideration [16].

Current research has further explored complex flow phenomena in eccentric geometries, including bioconvection flows with triple stratification [17], irreversibility analysis in porous media [18], and radiative mixed convection in hybrid nanofluids

[19]. Furthermore, using an approximation of the velocity distribution, the eccentric annulus was treated as a slit with variable height in order to assess the loss coefficient for power-law and Bingham fluids [20]. Furthermore, the eccentric or concentric annular duct provided a computational solution to the fully developed Casson model problem [5]. The FDM was also used to solve the hydrodynamic entrance region problem for the eccentric annulus [21]. Other references have investigated related aspects, such as non-Newtonian flow properties [22], slot-flow approximations for eccentric annuli [23] and viscoplastic fluid dynamics in annular geometries [24]. More recent advancements in non-Newtonian fluid dynamics, such as non-Fourier diffusion models [25], entropy generation in 3D flows [26], magnetohydrodynamic Sutterby nanofluid flows [27], stratified Carreau nanofluid studies [28], the dynamics of chemically reactive magneto-hybrid nanomaterials with heat radiation in porous media [29] and radiative convective flows with magnetic fields [30], underscore the ongoing relevance of such studies.

Therefore, this study attempts to fill a gap in the literature by proposing a numerical solution to the Casson model's entrance problem in eccentric or concentric annuli ducts. The fluid velocity and pressure gradients were evaluated at the entrance and fully developed regions and the ratios between them were calculated. In addition, comparisons of the calculated values with those found in the literature revealed a high degree of consistency. In contrast to previous studies that focused primarily on the fully developed flow or simpler concentric geometries, this work introduces a novel approach by tackling the complex entrance region dynamics of Casson fluid flow within eccentric annuli using a finite difference method with a variable mesh size. This method, combined with the adoption of bipolar coordinates, enables a more precise resolution of the non-uniform flow fields inherent to eccentric configurations. This challenge was often overlooked in previous studies that focused on Newtonian fluids or uniform annuli. Furthermore, the study's emphasis on the Casson fluid, a non-Newtonian model with yield stress relevant for industrial and biological applications, distinguishes it from traditional analyses, offering new insights into the pressure and velocity behaviors under varying radius ratios (S), relative eccentricities (e) and yield stress values (τ_D). By quantifying these parameters in the entrance region, which has been insufficiently explored in previous literature, this research provides a significant advance. When validated against established work, accuracy rates of 97.89% to 99.68% are achieved for fully developed regions, increasing the reliability of design predictions for engineering systems.

Furthermore, this paper is divided into five sections. Section 2 provides the problem formulation and solution, while Section 3 introduces the numerical model and application. Sections 4 and 5 include the results, along with discussion and conclusion, respectively.

2. Problem Formulation

2.1. **Governing Equations.** Figure 1 shows the geometry of the problem. The eccentric annulus comprises two cylindrical surfaces with inner radius R_1 and outer radius R_2, which are offset by the eccentricity d. It does not involve rotating disks or mechanical transmission; the study focuses on the transition of steady laminar flow from the entrance region to the fully developed region. In the entrance region of an eccentric or concentric annulus, the fluid is assumed to be laminar, steady, incompressible and non-Newtonian, in particular a Casson fluid with constant physical properties. The continuity (2.1) and momentum equations (2.2)–(2.4) in Cartesian

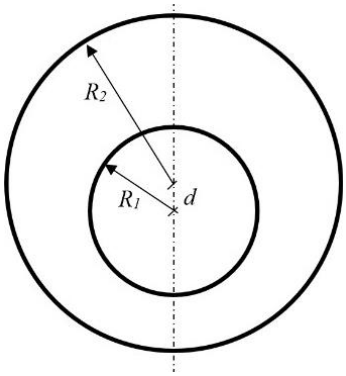

Figure 1. Geometry of studied eccentric annulus

coordinates are transformed into bipolar coordinates for the eccentric geometry, with the focus on the axial flow (z-direction) as the primary, with transverse components (u, v) secondary per boundary layer assumptions [21, 31]. Neglecting the body forces, the continuity equation is represented as follows

$$\nabla \cdot \mathbf{w} = 0, \tag{2.1}$$

while the momentum equations are given by

$$\rho\left(u\frac{\partial u}{\partial x}+v\frac{\partial u}{\partial y}+w\frac{\partial u}{\partial z}\right)=-\frac{\partial p}{\partial x}+\frac{\partial}{\partial x}\left(2\mu\frac{\partial u}{\partial x}\right)+\frac{\partial}{\partial y}\left[\mu\left(\frac{\partial v}{\partial x}+\frac{\partial u}{\partial y}\right)\right]+\frac{\partial}{\partial z}\left[\mu\left(\frac{\partial w}{\partial x}+\frac{\partial u}{\partial z}\right)\right], \tag{2.2}$$

$$\rho\left(u\frac{\partial v}{\partial x}+v\frac{\partial v}{\partial y}+w\frac{\partial v}{\partial z}\right)=-\frac{\partial p}{\partial y}+\frac{\partial}{\partial x}\left[\mu\left(\frac{\partial u}{\partial y}+\frac{\partial v}{\partial x}\right)\right]+\frac{\partial}{\partial y}\left[2\mu\frac{\partial v}{\partial y}\right]+\frac{\partial}{\partial z}\left[\mu\left(\frac{\partial w}{\partial y}+\frac{\partial v}{\partial z}\right)\right], \tag{2.3}$$

$$\rho\left(u\frac{\partial w}{\partial x}+v\frac{\partial w}{\partial y}+w\frac{\partial w}{\partial z}\right)=-\frac{\partial p}{\partial z}+\frac{\partial}{\partial x}\left[\mu\left(\frac{\partial u}{\partial z}+\frac{\partial w}{\partial x}\right)\right]+\frac{\partial}{\partial y}\left[\mu\left(\frac{\partial w}{\partial y}+\frac{\partial v}{\partial z}\right)\right]+\frac{\partial}{\partial z}\left[2\mu\frac{\partial w}{\partial z}\right], \tag{2.4}$$

where the apparent viscosity, μ, is given by:

$$\mu = \left(K_c + \left(\frac{\tau_0}{\sqrt{\left(\frac{\partial w}{\partial x}\right)^2 + \left(\frac{\partial w}{\partial y}\right)^2}} \right)^{\frac{1}{2}} \right)^2, \tag{2.5}$$

where K_c is the model viscosity and τ_0 is the yield stress.

Considering the no-slip condition at the walls, and due to symmetry, the solution can be evaluated for only one-half of the eccentric annulus. This yields the following

$$\begin{aligned} &\text{Inner conditions:} \quad w = w_e, \quad u = v = 0, \\ &\text{Boundary conditions:} \quad w = u = v = 0, \\ &\text{Symmetry lines:} \quad \frac{\partial w}{\partial n} = \frac{\partial u}{\partial n} = \frac{\partial v}{\partial n} = 0. \end{aligned}$$

2.2. **Bipolar Coordinates System Formulation.** It is convenient to represent the governing equations in the bipolar coordinate system, (ξ, η, z) when analyzing flow in eccentric annuli. The eccentric annulus, which consists of sets of orthogonal circles, is represented by the two coordinates (ξ, η), while the z-axis is perpendicular to the paper's plane. The walls of the eccentric annulus are represented by $\xi = \xi_1$ and $\xi = \xi_2$. Moreover, the relation between the rectangular coordinates x, y, z and the bipolar coordinates ξ, η, z is given by [22] as:

$$\begin{aligned} &\left(\frac{x}{a}\right)^2 + \left(\frac{y}{a} - \coth\xi\right)^2 = \operatorname{csch}^2\xi, \quad \text{for } -\infty < \xi < +\infty, \\ &\left(\frac{x}{a} - \cot\eta\right)^2 + \left(\frac{y}{a}\right)^2 = \csc^2\eta, \quad \text{for } 0 < \eta < 2\pi, \\ &x = \frac{a\sinh\xi}{\psi}, \quad y = -\frac{a\sin\eta}{\psi}, \end{aligned}$$

where

$$\begin{aligned} &z = za, \quad R_1\sinh\xi_1 = R_2\sinh\xi_2, \quad \psi = \cosh\xi - \cos\eta, \\ &\xi_1 = \cosh^{-1}\left(\frac{1 - S^2 - M^2}{2SM}\right), \\ &\xi_2 = \cosh^{-1}\left(\frac{1 - S^2 + M^2}{2M}\right). \end{aligned} \tag{2.6}$$

The relative displacement $M = \frac{d}{R_2}$ or the relative eccentricity $e = \frac{d}{R_2 - R_1}$, with the radius ratio $S = \frac{R_1}{R_2}$, are the two factors that characterize the annulus. Using the values of S, e, and M, which are between 0 and 1.0, the preceding 2.6 can be used to calculate ξ_1 and ξ_2. Due to the problem's symmetry, only one half, which lies between $\eta = 0$ and $\eta = \pi$, is taken into consideration. The bipolar coordinate system is explained in further detail in [31, 32], where the continuity equation and the three

momentum equations can be expressed as:

$$\frac{\partial}{\partial\xi}(hu)+\frac{\partial}{\partial\eta}(hv)+\frac{\partial}{\partial z}(h^2w)=0, \tag{2.7}$$

$$\begin{aligned}
\rho\left(\frac{u}{h}\cdot\frac{\partial u}{\partial\xi}+\frac{v}{h}\cdot\frac{\partial u}{\partial\eta}+w\frac{\partial u}{\partial z}\right)=&-\frac{\partial p}{\partial\xi}+\frac{1}{h}\cdot\frac{\partial}{\partial\xi}\left[2\frac{\mu}{h^2}\cdot\frac{\partial(hu)}{\partial\xi}\right]+\frac{1}{h}\cdot\frac{\partial}{\partial\eta}\left[\frac{\mu}{h^2}\left(\frac{\partial(hv)}{\partial\xi}+\frac{\partial(hu)}{\partial\eta}\right)\right]\\
&+\frac{1}{h}\cdot\frac{\partial}{\partial z}\left[\mu\left(\frac{\partial w}{\partial\xi}+\frac{\partial(hu)}{\partial z}\right)\right],\\
\rho\left(\frac{u}{h}\cdot\frac{\partial v}{\partial\xi}+\frac{v}{h}\cdot\frac{\partial v}{\partial\eta}+w\frac{\partial v}{\partial z}\right)=&-\frac{\partial p}{\partial\eta}+\frac{1}{h}\cdot\frac{\partial}{\partial\xi}\left[\frac{\mu}{h^2}\left(\frac{\partial(hv)}{\partial\xi}+\frac{\partial(hu)}{\partial\eta}\right)\right]+\frac{1}{h}\cdot\frac{\partial}{\partial\eta}\left[2\frac{\mu}{h^2}\cdot\frac{\partial(hv)}{\partial\eta}\right]\\
&+\frac{1}{h}\cdot\frac{\partial}{\partial z}\left[\mu\left(\frac{\partial w}{\partial\eta}+\frac{\partial(hv)}{\partial z}\right)\right],\\
\rho\left(\frac{u}{h}\cdot\frac{\partial w}{\partial\xi}+\frac{v}{h}\cdot\frac{\partial w}{\partial\eta}+w\frac{\partial w}{\partial z}\right)=&-\frac{\partial p}{\partial z}+\frac{1}{h^2}\cdot\frac{\partial}{\partial\xi}\left[\mu\left(\frac{\partial w}{\partial\xi}+\frac{\partial(hu)}{\partial z}\right)\right]\\
&+\frac{1}{h^2}\cdot\frac{\partial}{\partial\eta}\left[\mu\left(\frac{\partial(hv)}{\partial z}+\frac{\partial w}{\partial\eta}\right)\right]+\frac{\partial}{\partial z}\left[2\mu\frac{\partial w}{\partial z}\right],
\end{aligned}$$

where

$$\mu=\left(K_c+\left(\frac{\tau_0 h}{\sqrt{\left(\frac{\partial w}{\partial x}\right)^2+\left(\frac{\partial w}{\partial y}\right)^2}}\right)^{1/2}\right)^2,\quad h=\frac{a}{\cosh\xi-\cos\eta}. \tag{2.8}$$

Hughes and Gaylord [33] provided the general orthogonal curvilinear coordinate formulas along with the required bipolar coordinate system for (2.7) to (2.8) and (2.5). Feldman et al. [21] proposed an order of magnitude analysis that follows the boundary layer assumptions assuming that the length of the entrance region to the duct hydraulic diameter ratio is significantly greater than 1. As a result, the model assumes a uniform entrance velocity profile and disregards the transverse pressure gradient. Additionally, the continuity equation is unaffected by the order of magnitude analysis, and all three scalar components are replaced by a simplified form of the axial momentum equation. In bipolar coordinates, the continuity equation and the three reduced momentum equations are

$$\frac{\partial}{\partial\xi}(hu)+\frac{\partial}{\partial\eta}(hv)+\frac{\partial}{\partial z}(h^2w)=0, \tag{2.9}$$

$$\rho\left(\frac{u}{h}\cdot\frac{\partial w}{\partial\xi}+\frac{v}{h}\cdot\frac{\partial w}{\partial\eta}+w\frac{\partial w}{\partial z}\right)=-\frac{dp}{dz}+\frac{1}{h^2}\left[\frac{\partial}{\partial\xi}\mu\frac{\partial w}{\partial\xi}+\frac{\partial}{\partial\eta}\mu\frac{\partial w}{\partial\eta}\right]. \tag{2.10}$$

The pressure gradient, $\frac{dp}{dz}$, is a total derivative and a function of only z, whereas u, v, and w in (2.9) and (2.10) are functions of ξ, η, and z, respectively. Given that the pressure gradient is only one of three unknown of velocitycomponents, a comprehensive mathematical model cannot be formed by (2.9) and (2.10) only. Similar challenges existed when Carlson and Hornbeck [34] solved the hydrodynamic entrance region of

a square-sectioned duct. By assuming that all transverse flow was conducted along straight lines that crossed the center of the duct, they were able to create a relationship between the two transverse velocity components in the square cross-section. As stated in Feldman et al. [21], a brief examination of the process that causes transverse flow in an annular duct provides important insights into its behavior. When a flow with a uniform axial profile and no transverse components enters a circular tube, the flow near the wall is retarded, and the transverse flow is directed radially and symmetrically toward the center. Similarly, external axial flow along a cylinder's lateral surface causes radially symmetrical transverse flow outward from the cylinder's center. In a concentric annulus formed by inserting a cylinder inside the tube, the two transverse flows collide and vanish along a surface of revolution. If we consider two boundary layers growing concurrently along the two walls, then this surface lies between the two boundary layers, and the cylindrical surface with constant radius serves as a good approximation. The ridge of maximum axial velocities for fully developed flow is cut by this cylinder. This representation is accurate at axial points far from the duct inlet and reasonable near the duct inlet.

Similar mechanisms operate in the eccentric case as well. The expected paths of the transverse flow were described in Feldman et al. [21]. It would follow the radial lines originating from its surface if the transverse flow of either surface could act independently of the other one. The transverse flows of each surface, however, are forced to curve away from their respective radial lines by the presence of the other surface. As they approach each other, the two flows follow paths that tend to transfer flow from the narrower side of the annulus to the wider side of the annulus. The cylindrical surface that intersects the ridge of the maximum axial velocity for the fully developed flow can be used to approximate the surface along which the two transverse flows merge under conditions similar to those proposed for the concentric case. This surface can be represented mathematically by one with a constant radius, R^*. However, as absolute eccentricity increases, this curve significantly deviates from a constant radius, adopting an egg-shaped form. Fortunately, as will be shown later in this paper, the solution's sensitivity to the transverse flow prescription is negligible. For a concentric annulus, the classical closed-form representation of R^* is

$$R^* = R_2 \frac{\sqrt{1-S^2}}{\ln(1/S^2)}, \quad \text{for } e \neq 0.9,\ S \neq 0.1,$$

$$R^* = \frac{R_2}{2}, \quad \text{for } e = 0.9,\ S = 0.1.$$

For all but the most eccentric geometry ($e = 0.9$, $S = 0.1$), this representation is also used to approximate R^*. The circle formed by the R^* curve in this extreme case does not contain the center of the curve defining the outer wall due to the use of the chosen R^* representation. Consequently, the model fails because the radial lines originating from the inner and outer walls do not intersect as shown. R^* is therefore assumed in this case to be equal to 50% of the outer wall's radius [21].

Based on the above description and assumptions, a mathematical relationship for the transverse velocity ratio, v/u, was developed as

$$\frac{u}{v} = F\frac{(t_2 - t_1)}{1 + t_1 t_2}, \quad \xi \neq \xi^*, \tag{2.11}$$

where

$$F = \frac{\operatorname{csc}(\xi_2) - \operatorname{csch}(\xi^*)}{\operatorname{csch}(\xi) - \operatorname{csch}(\xi^*)}, \quad \text{for } \xi < \xi^* \quad \text{or} \quad F = \frac{\operatorname{csc}(\xi_1) - \operatorname{csch}(\xi^*)}{\operatorname{csch}(\xi) - \operatorname{csch}(\xi^*)}, \quad \text{for } \xi > \xi^*, \tag{2.12}$$

$$t_2 = \frac{H(1-S)\sinh(\xi)}{0.5\sinh(\xi_2)\cot(\eta) - H(1-S)\sin(\eta)}, \quad \xi^* = \sinh^{-1}\left(\frac{a}{R^*}\right), \tag{2.13}$$

$$t_1 = \frac{H(1-S)\sin(\eta)}{H(1-S)\sinh(\xi) - \cosh(\xi_2)} \quad \text{or} \tag{2.14}$$

$$t_1 = \frac{H(1-S)\sin(\eta)}{H(1-S)\sinh(\xi) - \cosh(\xi_1)}, \quad \text{for } \xi > \xi^*,$$

$$H = \frac{0.5\sinh(\xi_2)}{(1-S)(\cosh(\xi) - \cos(\eta))}, \tag{2.15}$$

$$\text{for} \quad \xi = \xi^*, \quad u = 0. \tag{2.16}$$

A complete model of the hydrodynamic entrance region is provided by (2.9), (2.10), and (2.11) to (2.16) along with zero-velocity boundary conditions and a uniform inlet velocity profile. However, several hydrodynamic entrance region solutions, such as those for parallel plates by Bodoia [35], a circular tube by Hornbeck [36], and a square duct by Carlson and Hornbeck [34], have also used the integral form of the continuity equation as noted by Hornbeck [36] and Feldman and Hornbeck [21]. These solutions all contain the differential version of the continuity equation, a reduced axial momentum equation in which the pressure gradient is a total derivative, and, in the case of the square duct, a transverse flow model, making them identical to consistent with the present model. Nevertheless, the integral form of the continuity equation is mathematically redundant because it can simply be produced by applying the divergence theorem to the differential form. This form is not represented in all nodal regions close to the duct walls in the finite difference solution, avoidingredundancy. The integral continuity equation has the following bipolar coordinate form

$$\frac{\pi}{2}a^2(1-S)^2 w_e \operatorname{csch}^2(\xi_2) = \int_0^{\pi}\int_{\xi_2}^{\xi_1} w h^2 d\xi d\eta, \tag{2.17}$$

where w_e represents the volume rate of flow per unit of cross-sectional area, was calculated using the average axial velocity. Equation (2.17), which imposes a physical constraint and excludes the transverse velocity components, is particularly useful [21].

2.3. **Method of Solution.** Here, it is more convenient to represent the variables and parameters in dimensionless form for the model as

$$\begin{aligned} &U = \frac{uR_e}{w_e}, \quad V = \frac{vR_e}{w_e}, \quad W = \frac{w}{w_e}, \quad P = \frac{p - p_e}{\rho w_e^2}, \quad Z = \frac{z}{D_h R_e}, \quad H = \frac{h}{D_h}, \\ &\mu_r = \frac{\mu R_e}{\rho w_e D_h}, \quad \tau_D = \frac{\tau_o R_e}{\rho w_e^2} \quad \text{and} \quad R_e = \frac{\rho}{k_c^2} w_e D_h, \end{aligned} \tag{2.18}$$

where p_e is the pressure at the entrance, R_e is the Reynolds number, τ_D is the dimensionless yield stress, and D_h is the hydraulic diameter given by

$$D_h = 2(R_2 - R_1) = 2a(1 - S)\operatorname{csch}\xi_2. \tag{2.19}$$

The following equations are obtained by substituting (2.18) and (2.19) into (2.5), (2.9), (2.10) and (2.11) to (2.17).

Assumed by the dimensionless form of viscosity

$$\mu_r = \left(K_c + \left(\frac{H\tau_D}{\sqrt{\left(\frac{\partial w}{\partial x}\right)^2 + \left(\frac{\partial w}{\partial y}\right)^2}} \right)^{\frac{1}{2}} \right)^{1/2}.$$

The dimensionless forms continuity and momentum equations now take the form

$$\frac{\partial}{\partial \xi}(HU) + \frac{\partial}{\partial \eta}(HV) + \frac{\partial}{\partial z}(H^2 W) = 0,$$

$$\frac{U}{H} \cdot \frac{\partial W}{\partial \xi} + \frac{V}{H} \cdot \frac{\partial W}{\partial \eta} + W\frac{\partial W}{\partial z} = -\frac{dP}{dZ} + \frac{1}{H^2}\left[\frac{\partial}{\partial \xi}\left(\mu_r \frac{\partial W}{\partial \xi} \right) + \frac{\partial}{\partial \eta}\left(\mu_r \frac{\partial W}{\partial \eta} \right) \right]. \tag{2.20}$$

All other variables in (2.12) to (2.16) are already dimensionless due to the dimensionless nature of u and v in (2.18), which makes u/v equal to U/V. Thus, (2.11) through (2.16) are not altered, except that (2.11) and (2.16) are updated to:

$$\frac{U}{V} = F\frac{t_2 - t_1}{1 + t_1 t_2}, \quad \text{for } \xi \neq \xi^*, \quad \text{and} \quad U = 0, \quad \text{for } \xi = \xi^*. \tag{2.21}$$

Then, the dimensionless integral form of the continuity equation (2.17) is as follows

$$\frac{8(1 - S)}{\pi(1 + S)} \int_0^{\pi} \int_{\xi_2}^{\xi_1} W H^2 \, d\xi \, d\eta = 1.0, \tag{2.22}$$

which employs the trapezoidal rule for the double integral. Moreover, the dimensionless boundary conditions are:

$$\begin{aligned} U = V = W = 0, &\quad \text{at } \xi = \xi_1 \text{ and } \xi = \xi_2, \\ W = 1, &\quad \text{at } Z = 0, \\ \frac{\partial W}{\partial \eta} = 0, &\quad \text{at } \eta = 0 \text{ and } \eta = \pi. \end{aligned}$$

3. Numerical Model and Implementation

3.1. **Numerical Model.** A numerical marching technique that divides the hydrodynamic entrance region into a number of parallel planes that are perpendicular to the z-axis provides a finite difference solution to the model. To create a finite difference grid that covers half of the symmetric annular cross section, sets of constant ξ curves (with index i) and constant η curves (with index j) are used to segment off the region defined by $\xi_1 \le \xi \le \xi_2$. This grid was selected to be fine enough to produce solutions with acceptably low truncation errors without requiring excessive computational cost or storage. Starting from either wall, the ξ interval from ξ_1 to ξ^* and the one from ξ^* to ξ_2 is divided into m variable segments. The steep velocity gradients near the walls are accommodated very fine grid spacing. The η interval from 0 to π is divided into l equal segments. Therefore, there are $(2m-1)l$ interior grid points, with indices (i,j), for which values of the three velocity components, $U_{i,j}$, $V_{i,j}$, and $W_{i,j}$, are required, while $(l+1)$ points on each ξ boundary for which have all values of $U_{i,j}$, $V_{i,j}$, and $W_{i,j}$ set to zero. Non-uniform step lengths in the ξ direction (variable mesh size), uniform step lengths in the η direction, and non-uniform step lengths in the z direction are each represented by $\Delta\xi_i$ (where $\Delta\xi_i = \xi_{i+1} - \xi_i$), $\Delta\eta$, and Δz, respectively. Consequently, the continuity equation, using central difference, takes the following form

$$
\begin{aligned}
&\frac{H_{i,j-1}U_{i,j-1,k+1} - H_{i-1,j}U_{i-1,j,k+1} - H_{i-1,j-1}U_{i-1,j-1,k+1} + H_{i,j}U_{i,j,k+1}}{2\Delta\xi_{i-1}} \\
&+ \frac{-H_{i,j-1}V_{i,j-1,k+1} + H_{i-1,j}V_{i-1,j,k+1} - H_{i-1,j-1}V_{i-1,j-1,k+1} + H_{i,j}V_{i,j,k+1}}{2\Delta\eta} \\
&+ \frac{H^2_{i,j}W_{i,j,k+1} + H^2_{i-1,j}W_{i-1,j,k+1} + H^2_{i,j-1}W_{i,j-1,k+1} + H^2_{i-1,j-1}W_{i-1,j-1,k+1}}{4\Delta z} \\
&- \frac{H^2_{i,j}W_{i,j,k} + H^2_{i-1,j}W_{i-1,j,k} + H^2_{i,j-1}W_{i,j-1,k} + H^2_{i-1,j-1}W_{i-1,j-1,k}}{4\Delta z} = 0,
\end{aligned} \tag{3.1}
$$

while the momentum equation in the finite difference form is:

(3.2)

$$
\begin{aligned}
&\frac{U_{i,j,k}}{H_{i,j}}\left(\frac{W_{i+1,j,k+1}}{d_2\left(\Delta\xi_i^2\right)} - \frac{W_{i-1,j,k+1}}{d_2\left(\Delta\xi_{i-1}^2\right)} + \frac{d_3 W_{i,j,k+1}}{d_2}\right) + \frac{V_{i,j,k}}{H_{i,j}}\left(\frac{W_{i,j+1,k+1} - W_{i,j-1,k+1}}{2\Delta\eta}\right) \\
&+ \frac{W_{i,j,k}}{\Delta z}\left(W_{i,j,k+1} - W_{i,j,k}\right) \\
&= -\frac{dP}{dZ} + \frac{1}{H^2_{i,j}}\left[\frac{\mu_{r_{i+1/2},j,k+1}(W_{i+1,j,k+1} - W_{i,j,k+1})}{d_1\left(\Delta\xi_i\right)} - \frac{\mu_{r_{i-1/2},j,k+1}(W_{i,j,k+1} - W_{i-1,j,k+1})}{d_1\left(\Delta\xi_{i-1}\right)}\right] \\
&+ \frac{1}{H^2_{i,j}}\left[\frac{\mu_{r_{i,j+1/2},k+1}(W_{i,j+1,k+1} - W_{i,j,k+1}) + \mu_{r_{i,j-1/2},k+1}(W_{i,j,k+1} - W_{i,j-1,k+1})}{\Delta\eta^2}\right],
\end{aligned}
$$

where

$$
d_1 = \frac{\Delta\xi_i + \Delta\xi_{i-1}}{2}, \quad d_2 = \frac{1}{\Delta\xi_i} + \frac{1}{\Delta\xi_{i-1}}, \quad d_3 = \frac{1}{\Delta\xi_{i-1}^2} - \frac{1}{\Delta\xi_i^2}. \tag{3.3}
$$

3.2. **Problem Implementation.** The previously obtained results were coded in MATLAB [37]. However, the established difference scheme generates a system of linear algebraic equations in V, W, and $\frac{dP}{dZ}$. Subsequently, a set of $(2m+1)(l+1)+1$ simultaneous linear algebraic equations in W and $\frac{dP}{dZ}$ are obtained by combining (2.22) with (3.1) and (3.2) for $i = 2$ to $2m-1$ and $j = 2$ to l. At the first plane beyond the inlet, the hydrodynamic model is solved independently of all subsequent planes. The solution of the second plane depends only on the solution of the first one, and the solution of the $(k+1)$-th plane depends only on the solution of the k-th plane, which is its direct predecessor. As a result, the entire hydrodynamic entrance region is resolved by successively solving each plane in turn. The matrix form of the linear algebraic equations is as follows

$$AX = B, \tag{3.4}$$

where X denotes the unknowns of the algebraic equations, A represents their coefficients, and B contains their residuals. Then the matrix form of (3.4) may be expressed in the following way

$$\begin{bmatrix} A_1 & A_2 \\ A_3 & A_4 \end{bmatrix} \cdot \begin{bmatrix} W \\ P \end{bmatrix} = \begin{bmatrix} B_1 \\ B_2 \end{bmatrix}, \tag{3.5}$$

where A_1 is a $(2m-1)\times(l+1)$ matrix that includes the coefficients of $W_{i,j}$ in (3.2), while A_2 contains the coefficients of P in (3.2) and A_3 has the coefficients of the axial velocity $W_{i,j}$ derived from the integral (2.22). Also,

$$A_4 = \begin{bmatrix} 0 & 0 \end{bmatrix}.$$

Additionally, B_1 is a $(2m-1)\times(l+1)$ vector representing the residuals of (3.2) whereas B_2 is the vector that represents the residuals of (2.22). In order to solve nonsingular linear systems with coefficient matrices, Keller [38] investigated the behavior of the bordering algorithm (3.5). This algorithm has been used to solve a broad class of differential equations boundary value problems that are discretized. The matrix form (3.5) can be split into the following two equations using this technique

$$A_1 W + A_2 P = B_1, \tag{3.6}$$

$$A_3 W + A_4 P = B_2. \tag{3.7}$$

In which, the unknown W may be put in the form

$$W = \bar{W} - \hat{W} P. \tag{3.8}$$

Then (3.6) may be written as

$$A_1(\bar{W} - \hat{W}P) + A_2 P = B_1, \tag{3.9}$$

i.e.,

$$A_1 \bar{W} + P(A_2 - A_1 \hat{W}) = B_1. \tag{3.10}$$

In order to eliminate P from (3.10), $\hat{W}$ is solved using

$$A_1\hat{W} = A_2, \tag{3.11}$$

and then $\bar{W}$ is obtained through solving

$$A_1\bar{W} = B_1. \tag{3.12}$$

However, the five-band system represented by (3.11) and (3.12) can be solved using the relaxation method to obtain both $\bar{W}$ and $\hat{W}$. The sparsity of matrix A_1 with many zero elements that are ignored during the solution steps makes this method appropriate for solving such systems. Therefore, the relaxation equation is expressed as

$$\alpha_{2i,j} = \frac{w_e}{a_{i,j}}\left(a_{i,j-1}\alpha_{2i,j-1} + a_{i,j+1}\alpha_{2i,j+1} + a_{i-1,j}\alpha_{2i-1,j} + a_{i+1,j}\alpha_{2i+1,j}\right) + (1 - w_e)\alpha_{1i,j}, \tag{3.13}$$

where α represents an element in the unknowns vectors $\bar{W}$ and $\hat{W}$, the subscript 1 means the known values of the variables 1, and the subscript 2 means the unknown values of the variables one. w_e is the relaxation factor, a is an element of matrix A_1, and b is an element of matrix A_2 or matrix B_1. Substitute (3.8) into (3.7) yields $A_3(\bar{W} - \hat{W}P) = B_2$. Then,

$$A_3\hat{W}P = A_3\bar{W} - B_2.$$

Equation (3.8) is used to determine W once P is known. Following the acquisition of all $W_{i,j}$ for a plane, the unknown $U_{i,j}$ and $V_{i,j}$ in the plane are all directly evaluated without any iterations using the numerical approximation to (3.1) and (2.21).

Starting with uniform axial velocity as a starting point, the flow in the annulus develops during the computations. The process is repeated at the next plane after resolving all unknowns at the $(k+1)$ plane. Repeating this process until the flow has fully developed, the relaxation parameter and the mesh size (axial and transverse) affect the stability and convergence speed. Furthermore, the model's finite difference equations are stable and consistent based on the available numerical findings. At a certain axial position on z, the truncation error of the difference scheme in (3.2) is $O(\Delta\xi + \Delta\eta^2)$. As a result, since $\Delta\xi$ and $\Delta\eta$ converge to zero, the difference equation (3.2) tends to the differential equation (2.20). The very tiny axial step size Δz, no larger than 0.25×10^5, was used near the inlet to account for the high axial gradients typically occurring at the duct entrance. Z was increased to a maximum of 0.001 increased.

4. Results and Discussion

The exact solution of Snyder and Goldstein [39] for the magnitude of discharge, Q, has been compared to the results of the current study while considering various values of e. As shown in Table 1, the comparison has examined a fully developed Newtonian fluid ($\tau_D = 0.0$), with $S = 0.5$. Different dimensionless parameters were considered

when calculating the discharge. Additionally, the accuracy of the current study was evaluated, revealing that agreement with the exact solution increases as e increases.

TABLE 1. Comparison of numerical results of discharge, Q with the exact solution of Synder and Goldstein

e	**Present Study**	**Snyder and Goldstein**	**Accuracy (%)**
$S = 0.5$			
0.2	0.051157	0.05226	97.88940
0.4	0.060041	0.06054	99.17575
0.6	0.073739	0.074052	99.57732
0.8	0.092061	0.09236	99.67627

Moreover, Table 2 compares the discharge values to those reported by Ateia et al. [5] at $S = 0.5$ considering various values of τ_D and e. As e is increased or decreased, the accuracy of the discharge values from the current study was evaluated and they were found to be consistent.

TABLE 2. Comparison of numerical results of discharge with the numerical solution of Ateia et al. for different values of τ_D

Reference	$\tau_D = 0$	$\tau_D = 0.025$	$\tau_D = 0.05$
Present study $S = 0.5$, $e = 0.2$	0.01197	0.020446	0.05116
[5]	0.01222	0.020845	0.05224
Accuracy (%)	97.9326	97.9542	98.0859
Present study $S = 0.5$, $e = 0.4$	0.01555	0.025390	0.06004
[5]	0.01537	0.025310	0.06049
Accuracy (%)	99.6839	99.2561	98.8289
Present study $S = 0.5$, $e = 0.6$	0.02068	0.032686	0.07398
[5]	0.02110	0.033011	0.07415
Accuracy (%)	99.0155	99.7707	98.0095
Present study $S = 0.5$, $e = 0.8$	0.02801	0.042758	0.09232
[5]	0.02859	0.043263	0.09237
Accuracy (%)	98.8327	99.9459	97.9713

This study's dimensionless entrance solution for pressure is contrasted with that of Feldman and Hornbeck [21]. Figure 2 depicts $e = 0.9$ and $S = 0.1$ for Newtonian fluid flow ($\tau_D = 0.0$), and the current findings are in good agreement with the earlier conclusion.

However, Figures 3, 4 and 5 examine the effect of S, e, and τ_D on the pressure gradient, respectively. Figure 3 illustrates the impact of the radius ratio ($S = 0.1, 0.5$ and 0.9) on the pressure gradient $-\frac{dP}{dZ}$ for constant values of relative eccentricity $e = 0.5$ and yield stress $\tau_D = 0$. It showed that as S decreases, the pressure gradient grows and quickly reaches its maximum. For $S = 0.1, 0.5$ and 0.9, the ratio

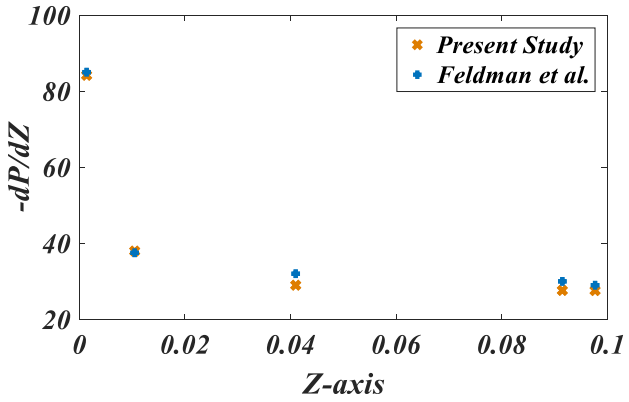

FIGURE 2. Comparison of the pressure gradient with the results of Feldman and Hornbeck, $e = 0.9$, $s = 0.1$ and $\tau_D = 0.0$

of pressure gradient values at $Z = 0$ to those at $Z = 1$ was 6.16, 7.90, and 17.65 times, respectively. This indicates how high the pressure gradient at the entrance region is. These significant increases (up to 17.65 times the fully developed values) stem from steep velocity gradients near the inlet. In Figure 3, the pressure gradient range expands as S increases, due to narrower annular gaps intensifying wall shear effects. Moreover, Figure 4 shows how the relative eccentricity ($e = 0.3, 0.5$ and 0.7) affects the pressure gradient $-\frac{dP}{dZ}$ for constant values of the radius ratio $S = 0.5$ and $\tau_D = 0$. As e decreases, the pressure gradient increases and quickly reaches its maximum. The pressure gradient values at $Z = 0$ were 50.52, 35.44, and 21.99 times greater than those at $Z = 1$ for $e = 0.3, 0.5$ and 0.7, respectively. This reflects the significant increase in the pressure gradient within the entrance region. For a Newtonian fluid $\tau_D = 0$, decreasing e narrows the annular gap, intensifying shear and resistance near the inner wall, which sharply elevates the pressure gradient at the inlet. Additionally, the pressure gradient $-\frac{dP}{dZ}$ for fixed values of the radius ratio $S = 0.5$ and the relative eccentricity $e = 0.5$ is affected by the yield stress $\tau_D = 0.0, 0.05, 0.5$ and 1, as shown in Figure 5. It increases as τ_D increases and gradually develops to its full value, which is expected given increased viscosity and resulting elevation in pressure gradient. For $\tau_D = 0.0, 0.05, 0.5$ and 1, the pressure gradient ratios at the entrance region relative to the steady fully developed zone were 10.64, 11.96, 14.83, and 16.86 times, respectively. This draws the designers' attention to the extremely high pressure in the entrance areas. For a Casson fluid, higher τ_D enhances the yield stress, requiring greater pressure to initiate flow, particularly at the entrance, where undeveloped flow amplifies viscous resistance.

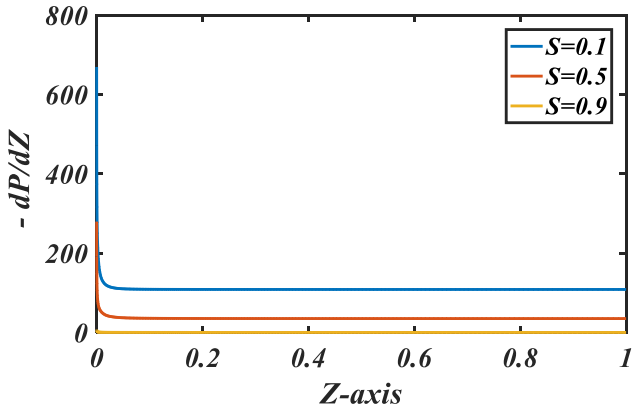

FIGURE 3. Distribution of the pressure gradient $(\frac{-dP}{dZ})$ versus Z for different values of S for $e = 0.5$ and $\tau_D = 0.0$

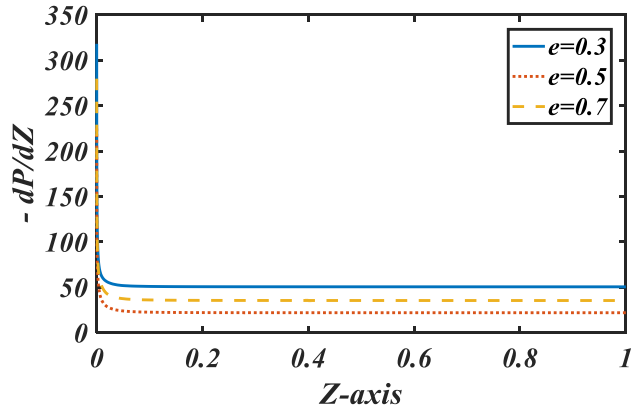

FIGURE 4. Distribution of the pressure gradient $(\frac{-dP}{dZ})$ versus Z for different values of e for $S = 0.5$ and $\tau_D = 0.0$

On the other hand, Figures 6, 7, and 8 demonstrate the effects of S, e, and τ_D on the axial velocity. Figure 6 depicts the impact of the radius ratio ($S = 0.1$, 0.5, and 0.9) on the axial velocity for constant values of the relative eccentricity $e = 0.5$ and the yield stress $\tau_D = 0.0$. As S decreases, the axial velocity increases to accommodate the increased area. The ratio of the entrance zone velocity to the fully developed one was 0.443626, 0.47152, and 0.437509 for $S = 0.1$, 0.5, and 0.9, respectively. For a Newtonian fluid $\tau_D = 0$, a lower S (smaller inner radius relative to the outer) widens

the annular gap, reducing flow resistance and boosting axial velocity near the entrance. However, as the flow develops, the velocity profile adjusts, leading to the observed ratios reflecting the transition from entrance to fully developed conditions.

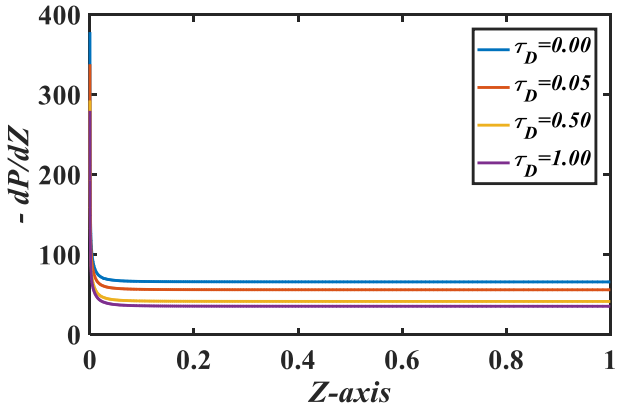

FIGURE 5. Distribution of the pressure gradient $(\frac{-dP}{dZ})$ versus Z for different values of $e = 0.5$ for $S = 0.5$ for different values of yield stress

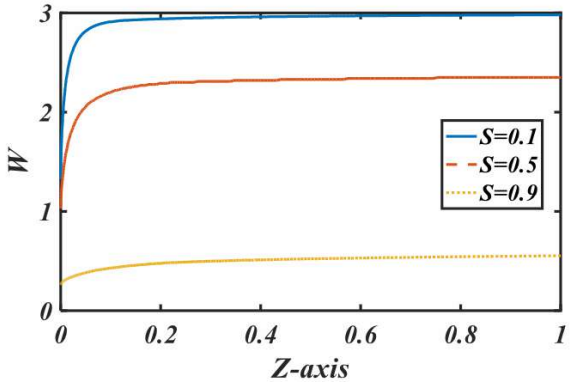

FIGURE 6. Distribution of the velocity, w versus Z for different values of S for $e = 0.5$ and $\tau_D = 0.0$

Additionally, Figure 7 shows the influence of relative eccentricity, $e = 0.3$, 0.5 and 0.7 on axial velocity for fixed values of radius ratio, $S = 0.5$, and yield stress, $\tau_D = 0$. It was found that as e increases (due to an increase in area), the axial velocity decreases. According to the results, the entrance zone velocity was 0.469391, 0.438141 and 0.437509 times its value in the fully developed region, respectively. For a Newtonian fluid $\tau_D = 0$, increasing e shifts the inner cylinder off-center, narrowing the gap on one side and widening it on the other. This asymmetry increases resistance

in the narrow region, reducing the axial velocity near the entrance despite the larger overall area, while the fully developed flow adjusts to a more uniform profile.

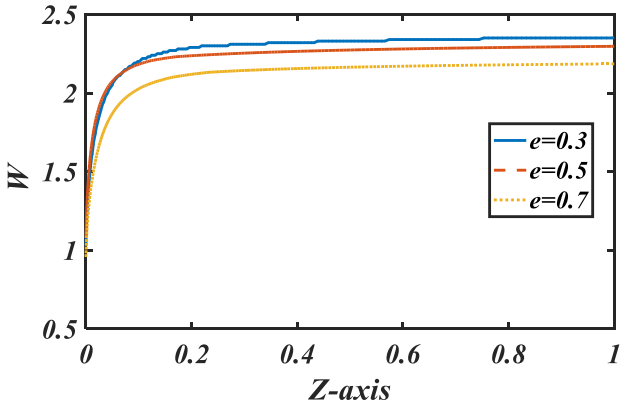

FIGURE 7. Distribution of the velocity, w versus Z for different values of e at $S = 0.5$ and $\tau_D = 0.0$

Furthermore, Figure 8 illustrates how the yield stress, $\tau_D = 0, 0.5$ and 1.0 affects the axial velocity for constant values of the radius ratio, $S = 0.1$ and relative eccentricity, $e = 0.9$. As τ_D increases, the viscosity rises and the axial velocity decreases correspondingly . The ratios of the entrance region velocity to the fully developed velocity were 0.496551714, 0.505679036 and 0.53654 for $\tau_D = 0, 0.5$ and 1.0, respectively. For a Casson fluid, higher τ_D increases the yield stress, enhancing resistance to flow initiation and reducing axial velocity, particularly near the entrance where flow is undeveloped. This effect is pronounced at low S and high e, as the narrow annular gap and eccentricity amplify viscous opposition, though the fully developed flow partially mitigates this reduction.

5. Concluding Remarks

The numerical findings were reported for the three-dimensional, steady, laminar fluid flow under hydrodynamically developed conditions. The fluid was assumed to be either Newtonian or non-Newtonian flowing through concentric or eccentric annulus duct. Computer software was developed that utilized two-dimensional storage and a marching strategy for solving differential equations line-by-line using the relaxation method. Subsequently, the effects of the axial position Z, the relative e, and the radius ratio S on the axial velocity profiles were studied.

Through this work, it was found that the pressure gradient is directly proportional to the yield stress; τ_D, and inversely proportional to both the radius ratio; S, and the relative eccentricity; e, whereas the axial velocity is inversely proportional to S, e, and

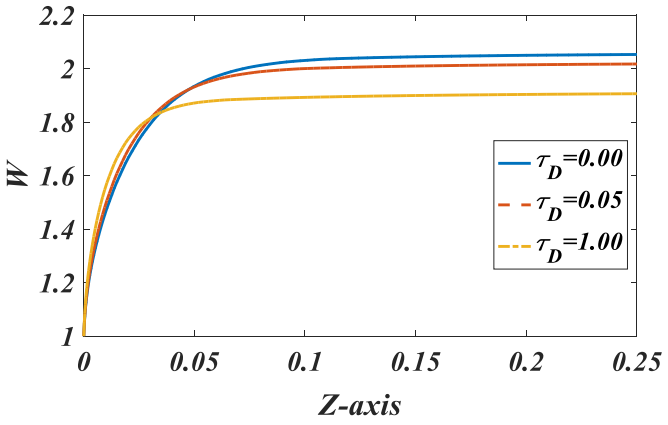

FIGURE 8. Distribution of the velocity, w versus Z for different values of τ_D at $e = 0.9$ and $S = 0.1$

τ_D. It was observed that the pressure gradient in the entrance region is significantly greater than the fully developed one. This ratio ranged from 6.16 for $S = 0.1$, $e = 0.5$ and $\tau_D = 0$ to 50.52 for $S = 0.5$, $e = 0.3$ and $\tau_D = 0$. In contrast to the pressure gradient, the axial velocity in the entrance region is consistently lower than in the fully developed zone,with its ratio varying between 0.437509 for $S = 0.5$, $e = 0.7$ and $\tau_D = 0$ and 0.53654 for $S = 0.1$, $e = 0.9$ and $\tau_D = 1$. This emphasizes the importance of investigating the entrance region for system designers.

The accuracy of the current results was compared to values reported in the literature showing good agreement.

Notations. We have used the following list of notations.

Dimensionless velocity components	U, V, W
Coefficient matrix	A
Velocity components	u, v, w
Coefficients sub-matrices	A_1, A_2, A_3
Velocity vector	W
Residuals vector	B
Intermediate matrices	$\bar{W}, \hat{W}$
Residuals sub-vectors	B_1, B_2
Volume rate of flow per unit	w_e
Hydraulic diameter	D_h
Eccentricity	d
Dimensionless z component	Z
Pressure gradient	$\frac{dp}{dz}$

Greek Symbols	
Model viscosity	K_c^2
Apparent viscosity	μ
Plane number	k
Dimensionless viscosity	μ_r
Relative eccentricity	M
Bipolar system coordinates	ξ, η, z
Dimensionless pressure	P
Fluid density	ρ
Entrance's pressure gradient	p_e
Yield stress	τ_D
Inner and outer radii	R_1, R_2
Distance between two points	Δ
Reynolds's number	R_e
Gradient derivative	∇
Radius ratio	S

References

[1] R. L. Batra and B. Jena, *Entrance region flow of blood in concentric annulus*, International Journal of Engineering Science **28**(5) (1990), 407–419. https://doi.org/10.1016/0020-7225(90)90006-5

[2] S. R. Nadiminti and A. Kandasamy, *Entrance effects of blood model Casson fluid in the concentric rings with inner ring rotation*, International Journal of Engineering and Advanced Technology **9**(1S5) (2019), 1–6. https://doi.org/10.35940/ijeat.A1045.1291S519

[3] M. C. A. Maia and C. A. Gasparetto, *A numerical solution for the entrance region of non-Newtonian flow in annuli*, Brazilian Journal of Chemical Engineering **20**(2) (2003), 201–211. https://doi.org/10.1590/S0104-66322003000200014

[4] M. Haciislamoglu and J. Langlinais, *Non-Newtonian flow in eccentric annuli*, Journal of Energy Resources Technology **112**(3) (1990), 163–169. https://doi.org/10.1115/1.2905753

[5] A. M. Ateia, M. E. Sayed and H. H. El-Din, *Magnetohydrodynamic flow and heat transfer of Casson in an eccentric annulus*, Alazhar Engineering International Conference, Cairo, 2003, 1–15.

[6] M. Katsuhisa, *Heat transfer in entry length of double pipes*, International Journal of Heat and Mass Transfer **2**(3) (1961), 240–251. https://doi.org/10.1016/0017-9310(61)90092-8

[7] A. Kandasamy and S. R. Nadiminti, *Entrance region flow in concentric annuli with rotating inner wall for Herschel-Bulkley fluids*, Int. J. Appl. Comput. Math. **1**(2) (2015), 235–249. https://doi.org/10.1007/s40819-015-0029-7

[8] S. R. Nadiminti and A. Kandasamy, *Entrance region flow in concentric annuli with rotating inner wall for Bingham fluid*, Journal of Computational and Applied Mechanics **11**(2) (2016), 137–157. https://doi.org/10.3311/PPme.8970

[9] A. Gupta and R. Sharma, *Exploration of temperature dependent thermophysical characteristics of yield exhibiting non-Newtonian fluid flow under gyrotactic microorganisms*, International Journal of Heat and Fluid Flow **92** (2022), 101–115. https://doi.org/10.1016/j.ijheatfluidflow.2021.108846

[10] R. Sharma and A. Gupta, *Heat transport in the convective Casson fluid flow with homogeneous-heterogeneous reactions in Darcy-Forchheimer medium*, Advances in Continuous and Discrete Models: Theory and Modern Applications **2023** (2023), 15–28. https://doi.org/10.1186/s13662-023-03759-0

[11] S. R. Nadiminti and A. Kandasamy, *Heat and mass transfer effects of Casson fluid in the entrance of concentric annuli with movement of walls*, Advances in Mathematics: Scientific Journal **9**(9) (2020), 6435–6446. https://doi.org/10.37418/amsj.9.9.1

[12] S. M. Venthan and I. J. Amalraj, *Numerical investigation of Bingham fluid flow in the entrance region of rotating annuli*, Trends in Mechanical and Biomedical Design: Select Proceedings of ICMechD 2019, Singapore, 2021, 499–518. https://doi.org/10.1007/978-981-15-4488-0_42

[13] N. Mitsuishi and Y. Aoyagi, *Non-Newtonian fluid flow in an eccentric annulus*, Journal of Chemical Engineering of Japan **6**(5) (1974), 402–408. https://doi.org/10.1252/jcej.6.402

[14] Y. Luo and J. M. Peden, *Flow of non-Newtonian fluids through eccentric annuli*, SPE Production Engineering **5**(1) (1990), 91–96. https://doi.org/10.2118/16692-PA

[15] M. P. Escudier, I. W. Gouldson, P. J. Oliveira and F. T. Pinho, *Effects of inner cylinder rotation on Laminar flow of a Newtonian fluid through an eccentric annulus*, International Journal of Heat and Fluid Flow **21**(1) (2000), 92–103. https://doi.org/10.1016/S0142-727X(99)00059-4

[16] J. M. Nouri and J. H. Whitelaw, *Flow of Newtonian and non-Newtonian fluids in an eccentric annulus with rotation of the inner cylinder*, International Journal of Heat and Fluid Flow **18**(2) (1997), 236–246. https://doi.org/10.1016/S0142-727X(96)00086-0

[17] A. A. Khan and S. Rehman, *Bioconvection flow of Prandtl nanomaterial due to stretched cylinder enclosed through Darcy-Forchheimer flow with triple stratification*, International Journal of Heat and Mass Transfer **185** (2022), 122–136. https://doi.org/10.1016/j.ijheatmasstransfer.2021.122136

[18] S. Iqbal and M. Farooq, *Irreversibility analysis of bioconvection nanofluid flow in a Darcy-Forchheimer porous medium induced by a rotating disk with thermal radiation*, Appl. Math. Model. **105** (2023), 130–145. https://doi.org/10.1016/j.apm.2022.10.008

[19] I. Siddique and S. Bukhari, *Exact solution of radiative flow on the mixed convection flow of hybrid nanofluid in a porous medium, Laplace transform technique for sustainable energy*, Renewable Energy **201** (2023), 159–172. https://doi.org/10.1016/j.renene.2022.11.086

[20] I. Tosun, S. Solmaz and C. Ozgen, *Loss coefficients in entrance region flows of Newtonian and non-Newtonian fluids in eccentric annuli*, Chemical Engineering Communications **131**(1) (1995), 207–224. https://doi.org/10.1080/00986449508936292

[21] E. E. Feldman and R. W. Hornbeck, *A numerical solution of Laminar developing flow in eccentric annular ducts*, International Journal of Heat and Mass Transfer **25**(2) (1982), 231–241. https://doi.org/10.1016/0017-9310(82)90009-6

[22] T. L. Guckes, *Laminar flow of non-Newtonian fluids in an eccentric annulus*, Journal of Engineering for Industry **97**(2) (1975), 498–502. https://doi.org/10.1115/1.3438611

[23] A. W. Iyoho and J. J. Azar, *An accurate slot-flow model for non-Newtonian fluid flow through eccentric annuli*, Society of Petroleum Engineers Journal **21**(5) (1981), 565–572. https://doi.org/10.2118/9447-PA

[24] P. Szabo and O. Hassager, *Flow of viscoplastic fluids in eccentric annular geometries*, Journal of Non-Newtonian Fluid Mechanics **45**(2) (1992), 149–169. https://doi.org/10.1016/0377-0257(92)85001-D

[25] R. Sharma and P. Kumar, *Application of non-Fourier double diffusions theories to the boundary-layer flow of a yield stress exhibiting fluid model*, Journal of Non-Newtonian Fluid Mechanics **305** (2023), 104–118. https://doi.org/10.1016/j.jnnfm.2022.104975

[26] M. I. Khan and S. Ahmed, *On the onset of entropy generation for a nanofluid with thermal radiation and gyrotactic microorganisms through 3D flows*, Appl. Math. Comput. **435** (2022), 127–139. https://doi.org/10.1016/j.amc.2022.127489

[27] N. Patel and V. Singh, *Modified heat and mass transmission models in the magnetohydrodynamic flow of sutterby nanofluid in stretching cylinder*, Int. J. Appl. Comput. Math. **9** (2023), 45–59. https://doi.org/10.1007/s40819-023-01503-6

[28] S. Rahman and T. Hussain, *Investigation of entropy generation in stratified MHD Carreau nanofluid with gyrotactic microorganisms under Von Neumann similarity transformations*, Phys. A **612** (2023), 128–142. https://doi.org/10.1016/j.physa.2023.128486
[29] N. Ahmed and Z. Shah, *Dynamics of chemical reactive on magneto hybrid nanomaterial with heat radiation due to porous exponential plate: Laplace transform technique for the heat and mass*, J. Comput. Appl. Math. **418** (2023), 114–129. https://doi.org/10.1016/j.cam.2022.114629
[30] M. Y. Malik and A. Hussain, *Radiation effects on rotating system free convective nanofluid unsteady flow with heat source and magnetic field*, Physica Scripta **97** (2022), 145–158. https://doi.org/10.1088/1402-4896/ac8b0f
[31] R. B. Bird, R. C. Armstrong, O. Hassager, C. F. Curtiss and S. Middleman, *Dynamics of polymeric liquids*, Vol. 1 and 2, Physics Today **31**(2) (1978), 54–57. https://doi.org/10.1063/1.2994977
[32] P. M. Morse and H. Feshbach, *Methods of Theoretical Physics*, McGraw-Hill Book Company, New York, 1953.
[33] W. F. Hughes and E. W. Gaylord, *Basic Equation of Engineering Science*, Schaum Publishing Co, New York, 1964.
[34] G. A. Carlson and R. W. Hornbeck, *A numerical solution for Laminar entrance flow in a square duct*, Journal of Applied Mechanics **40**(1) (1973), 25–30. https://doi.org/10.1115/1.3422937
[35] J. R. Bodoia, *The finite difference analysis of confined viscous flow*, PhD Thesis, Carnegie Institute of Technology, Pittsburgh, 1959.
[36] R. W. Hornbeck, *Laminar flow in the entrance region of a pipe*, Applied Scientific Research, Section A **13** (1964), 224–232. https://doi.org/10.1007/BF00382056
[37] MATLAB, Version R2023a, The MathWorks, Inc., Natick, MA, 2023.
[38] H. B. Keller, *The bordering algorithm and path following near singular points of higher nullity*, SIAM Journal on Scientific and Statistical Computing **4**(4) (1983), 573–582. https://doi.org/10.1137/0904039
[39] W. T. Snyder and G. A. Goldstein, *An analysis of fully developed Laminar flow in an eccentric annulus*, AIChE Journal **11**(3) (1965), 462–467. https://doi.org/10.1002/aic.690110319

[1]Faculty of Engineering, Eng. Mathematics and Physics Depatement,
Fayoum University,
Fayoum, 63514, Egypt
Email address: ama00@fayoum.edu.eg
ORCID iD: https://orcid.org/0009-0008-7890-8656

[2]Faculty of Engineering, Eng. Mathematics and Physics Depatement,
Fayoum University,
Fayoum, 63514, Egypt
Email address: ohg00@fayoum.edu.eg
ORCID iD: https://orcid.org/0000-0002-5064-1119